



Original Article

Investigation of molten fuel coolant interaction phenomena using real time X-ray imaging of simulated woods metal-water system



Avinash Kumar Acharya, Anil Kumar Sharma^{*}, Ch.S.S.S. Avinash, Sanjay Kumar Das, Lydia Gnanadhas, B.K. Nashine, P. Selvaraj

Fast Reactor Technology Group, Indira Gandhi Centre for Atomic Research, HBNI, Kalpakkam 603102, India

ARTICLE INFO

Article history:

Received 7 February 2017

Received in revised form

28 June 2017

Accepted 3 July 2017

Available online 14 July 2017

Keywords:

Image Processing

MFCI

Real Time X-Ray Imaging

Vapor Phase Imaging

ABSTRACT

In liquid metal fast breeder reactors, postulated failures of the plant protection system may lead to serious unprotected accidental consequences. Unprotected transients are generically categorized as transient overpower accidents and transient under cooling accidents. In both cases, core meltdown may occur and this can lead to a molten fuel coolant interaction (MFCI). The understanding of MFCI phenomena is essential for study of debris coolability and characteristics during post-accident heat removal. Sodium is used as coolant in liquid metal fast breeder reactors. Viewing inside sodium at elevated temperature is impossible because of its opaqueness. In the present study, a methodology to depict MFCI phenomena using a flat panel detector based imaging system (i.e., real time radiography) is brought out using a woods metal-water experimental facility which simulates the UO_2 -Na interaction. The developed imaging system can capture attributes of the MFCI process like jet breakup length, jet front velocity, fragmented particle size, and a profile of the debris bed using digital image processing methods like image filtering, segmentation, and edge detection. This paper describes the MFCI process and developed imaging methodology to capture MFCI attributes which are directly related to the safe aspects of a sodium fast reactor.

© 2017 Korean Nuclear Society, Published by Elsevier Korea LLC. This is an open access article under the CC BY-NC-ND license (<http://creativecommons.org/licenses/by-nc-nd/4.0/>).

1. Introduction

Studies related to the consequences of a molten fuel coolant interaction (MFCI) and safe retention of core debris after an MFCI are very important for the safety of plant personnel [1]. These data are helpful for development of a code to study the thermal hydraulics of severe accident scenarios in sodium fast reactors and to devise a system to retain the entire core debris. The present study is focused towards development of an imaging technique which will be able to depict the MFCI process consequent to severe accidents for sodium fast reactors. The technique, although developed for a particular experiment, can be used as a generic case of under sodium viewing.

The main challenges in imaging of an MFCI inside sodium are opacity, high temperature, and fast processes like solidification and fragmentation. Park et al [2] performed a quantitative visualization of the rapid fragmentation process of a high temperature melt drop

of tin (0.7 g at 1,000°C) employing continuous high speed X-ray and photography. Their developed methodology could capture large steam air pockets attached on the top of the melt drop in the explosion interaction zone. Matsuo et al [3] conducted an MFCI experiment with uranium alloy and water. They captured visual data using a high speed video camera and found it very useful in defining MFCI characteristics. They also described characteristics of the frontal velocity of the molten jet into a stagnant water pool. The visual images showed that the jet breakup length depends on the injection nozzle diameter and is independent of the jet penetration velocity. Hansson [4] studied the dynamics of the hot liquid (melt) droplet and the volatile liquid (coolant) in the Micro-Interactions in Steam Explosion Experiments (MISTEE) facility. They investigated well controlled, externally triggered, single-droplet experiments, using a high-speed visualization system with synchronized digital cinematography and continuous X-ray radiography. Magali et al [5] studied fuel coolant interaction phenomena for pressurized light water reactor in their KROTOS facility, France under the SERENA program. They developed a methodology to capture the interaction mechanisms between the different components of the system (the hot molten pool, the liquid water, the generated fragments, and

^{*} Corresponding author.

E-mail address: aksharma@igcar.gov.in (A.K. Sharma).

steam) from generated experimental data and calculation analysis. They were able to film the fragmentation of the melt within the test chamber using an X-ray radiography system. Potter et al [6], using microfocus X-ray imaging, studied defect formation in porcelain ceramics during drying. The onset of cracking, and hence the critical moisture content, can be established nondestructively by means of X-ray microfocus imaging. This imaging helped in precise determination of the time to formation of the first crack, even if that occurs internally. This is found to be more reliable than alternative optical means which rely upon externally visible fractures to determine the time to failure. It is concluded by them that MFX imaging can be used for online process control as a robust means of detecting the occurrence of fractures and voids within a body. Loewen et al [7] measured two dimensional distribution of molten lead interaction with water using application of continuous high and low energy X-rays. This technique depicted the three phases present in the process spatially and temporally. Munshi et al [8] described the role of tomography in void fraction measurement for a steady-state mercury loop. The paper reported very accurate measurements for void fractions present in the flow channel. The computed tomography-based imaging is useful in volumetric mapping of the process as compared to conventional radiography. However, the computed tomography technique is intricate in studying transient processes and is still evolving. Saksena et al [9] compared the void distribution in the riser leg of a mercury-nitrogen flow system obtained by gamma-ray tomography (experimental) and the FLUENT code (simulation). A comparison of the predicted and the experimental results shows that experimental numbers are consistently lower than numerical predictions.

From the above literature, it is clear that the determination of important attributes for MFCI, which are jet breakup length, fragmentation profile and noncondensable gas generation, is very important. However, the flow visualization for the MFCI process is scarce. Therefore, a woods metal water system has been used to develop and qualify the methodology to capture all attributes of MFCIs. The objective of the present study is to investigate the real time radiography potential in defining MFCI attributes for a woods metal water system and finally to develop imaging techniques for MFCIs in liquid sodium, which is an opaque medium.

2. Materials and methods

It is seen from literature that real time X-ray imaging is useful for depiction of an MFCI process. Hence, this study is performed for qualification of real time X-ray imaging system to understand the MFCI process. Water has been chosen as a simulant to replace sodium because of their similar attenuation curves generated by NIST [10,11].

2.1. Imaging principle

X-rays are a form of electromagnetic wave which penetrates through matter. They form images based on attenuation caused by the material. The attenuation depends upon the material density and length traveled by X-rays [12]. This decrease in X-ray energy is represented as follows:

$$I = I_0 \exp(-\mu t)$$

where I is intensity of the emergent radiation, I_0 is the source intensity, t is the thickness of homogeneous material, and μ is a characteristic of the material known as the linear absorption coefficient. The coefficient μ is constant for a given situation, but varies with the material and with the photon energy of the radiation. The units of μ are reciprocal length (for instance cm^{-1}). The

absorption coefficient of a material is sometimes expressed as mass-absorption coefficient (μ/ρ), where ρ is the density of the material. Both parameters can be tailored for the imaging requirements. The energy of the X-ray source is required to penetrate and form images in a system and is derived based on medium's steel equivalent thickness.

2.2. Experimental facility

The experimental setup consists of an X-ray imaging system and stainless steel (SS) cylindrical vessel integrated with a melt release system and is used to capture the images. The schematic diagram of experimental set up is depicted in Fig. 1.

2.2.1. Interaction vessel

A 7 mm thick SS cylindrical vessel with dimensions of 166 mm outer diameter (OD), 1 m length was used as an interaction tank for this experiment. A melt release system was integrated at the top of the cylindrical vessel. The system consists of an SS melt pot with a 600 W rated surface heater integrated with a high temperature SS valve. K-type thermocouples were used for temperature measurement of melt charge.

2.2.2. X-ray imaging system

The X-ray imaging system consists of a digital flat panel detector (DFPD) and constant potential 225 kV X-ray source. The screen size of the DFPD is 16 inches. The DFPD can acquire images with a maximum acquisition rate of 30 fps with 400 μm resolution. The attenuated X-ray energy corresponding to the object shape and density falls upon the DFPD. The X-rays which fall upon the scintillator screen of the DFPD are converted into different visible light intensities. These visible light intensities fall upon an amorphous silicon photo diode. The voltage formed as a function of X-ray intensities from a photodiode array forms the respective digitized 16 bit X-ray image. The DFPD sends image data to a personal computer over fiber optic communication via a frame grabber card. The DFPD is operated remotely through the device driver installed in the personal computer.

2.3. Procedure

The imaging of molten metal inside the interaction vessel is the main purpose for the present study. The simulant inside the vessel is imaged using the DFPD. The DFPD has been calibrated by an X-ray source with reference to the SS tank. After calibration, the DFPD is kept in such a way so that it covers the interaction region. Some 250 g of woods metal (melting point approximately 70°C) is heated up to 200°C and released into the water (at 30°C) filled in a tank with a remotely operated valve. The X-ray images were acquired at 25 fps with intervals of 40 milliseconds using a real time X-ray imaging system.

The acquired images contain important information regarding the complex process that takes place during the interaction. The raw images were captured, which depicts the presence of woods metal inside the water. From the raw images, it is difficult to interpret the process. Hence, these images were taken for image processing in sequence through image filtering, segmentation, and edge filtering for image analysis [13–15].

3. Results and discussion

X-ray images obtained using an X-ray source of 190 KeV, 5 mA exposure at different time intervals are shown in Fig. 2. These are acquired at 25 fps with 0.4 mm spatial resolution using a flat panel detector. These obtained raw images have poor contrast. It is

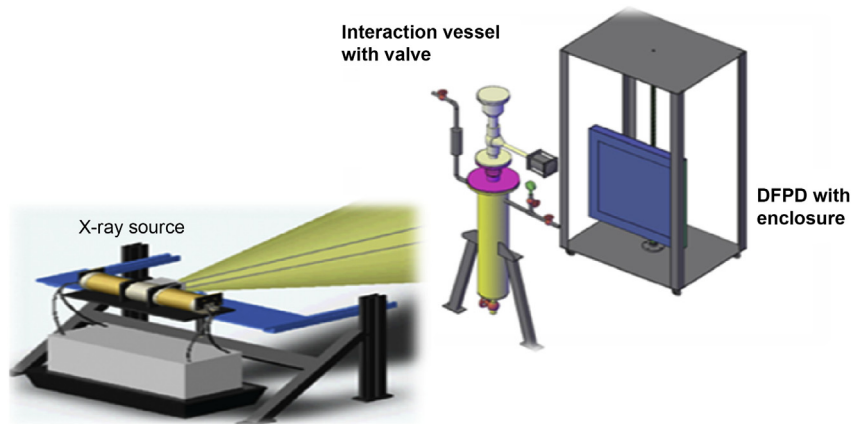


Fig. 1. Schematic of experimental set up. DFPD, digital flat panel detector.

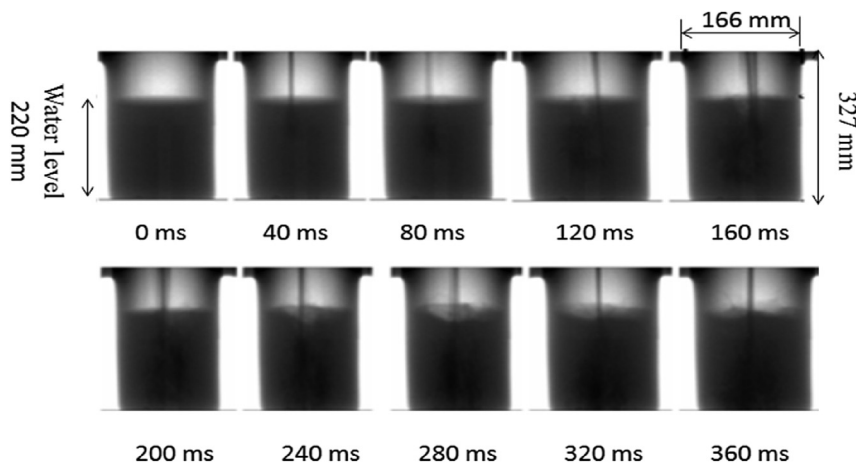


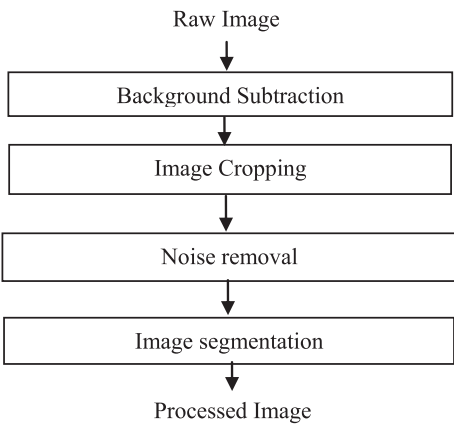
Fig. 2. Obtained X-ray images of woods metal water interaction.

impossible to identify features like jet breakup length, molten metal profile, and vapor phase formation with these images. The images depicted in Fig. 2 were enhanced using an image processing algorithm shown in Table 1. The algorithm was designed to enhance the raw images optimally using a Scilab Image processing design toolbox, Scilab image and video processing toolbox, and IPT3 in Scilab 5.5.2 environment (ESI company, France) [16].

3.1. Background subtraction

Background subtraction is performed on subsequent images from the image available at time $t = 0$ milliseconds. A simple arithmetic subtraction helps us to extract information hidden inside the water column. The subtracted image is depicted in Fig. 3. The subtracted images were analyzed and it was found that they

Table 1
Algorithm used for image enhancement.



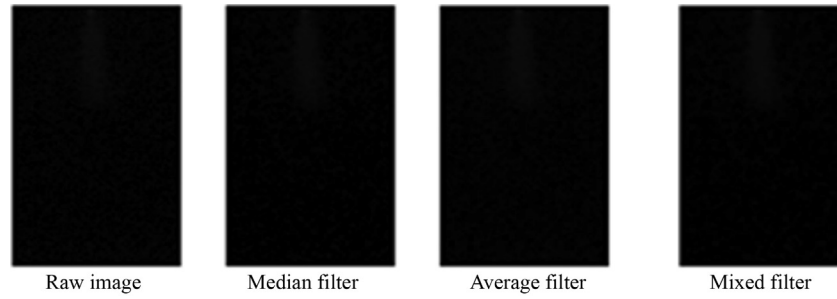


Fig. 3. Background subtracted images with different filters.

were heavily corrupted with noise.

3.2. Image cropping

Images were cropped to reduce the data set for the image. The main interest is to visualize the woods metal interaction pattern inside the water column. Therefore a 210×330 size cropping window operated with all the images.

3.3. Image filtering

Noise removal is crucial for image segmentation. The cropped images are improved using averaging, median, and mixed (combination of median and average) filters with all-ones (5×5) size matrix kernel. The idea of average filtering is to replace each pixel value in an image with the average value of its neighbors, including itself. This has the effect of eliminating pixel values which are unrepresentative of their surroundings. The median filter considers each pixel in the image corresponding to the chosen kernel. The median is calculated by pixel values obtained from the kernel in numerical order and then replacing the pixel with the middle pixel value of the kernel set. Fig. 3 depicts the raw image and filtered images obtained using mean, median, and mixed filters. The purpose of filtering is to suppress unwanted information which presents in the image in form of noise.

3.4. Quality metrics

The image quality measurement is quite a popular tool in present times. The best way to assess the quality of images is visual observation, but this varies with a person's ability. Mean opinion score has been used for many years but is very inconvenient and subjective. Mathematically developed quality metrics are available. These can predict objectively the performance of the proposed image processing algorithm for a set of input images. Absolute mean brightness error (AMBE), global contrast, gray level energy, maximum difference [17], and fractal dimension (FD) [18] were chosen over various quality metrics for evaluation of the proposed algorithm. The 29 processed images using average filtering, median filtering, and mixed filtering were evaluated based on quality metrics. These quality metrics are discussed below.

3.5. Gray level energy

The gray level energy (GLE) indicates how the grey levels are distributed. If an image has a GLE value approaching 1, then the image is said to be enhanced. It is given by:

$$E(x) = \sum_{i=0}^L p(i)^2$$

where $E(x)$ refers to the GLE and $p(i)$ refers to the probability distribution function of the histogram.

3.6. Global contrast

The global contrast value of an image is defined as the second central moment of its histogram divided by the total number of pixels in the image and is given by:

$$\text{Global contrast} = \frac{\sum_{i=0}^L (i - \mu)^2 * \text{Hist}(i)}{N}$$

where maximum gray level present in the image is L , mean of the image is μ , No. of occurrence of gray value i is $\text{Hist}(i)$.

3.7. Maximum difference

Maximum difference (MD) of the image is defined as the absolute difference between the original image at location (m, n) and the processed image at the same location (m, n) . The value of MD will be high for a good enhanced image. The expression for MD is given as:

$$\text{MD} = \text{Max}(|X(m, n) - Y(m, n)|)$$

where $X(m, n)$ denotes the pixel values of the original image at location (m, n) , $Y(m, n)$ denotes the pixel values of the processed image at the same location (m, n) .

3.8. AMBE

AMBE measures the deviation of the processed image mean from the input image mean. The AMBE value provides a sense of how the global appearance of the image has changed with respect to lower values. The expression for AMBE is given as:

$$\text{AMBE} = |\mu_p - \mu_i|$$

where μ_p is the mean of processed image and μ_i is the mean of the input image.

3.9. FD

FD is a useful feature for texture segmentation, shape classification, and image analysis. The FD is an important metric in evaluation of noise present in the digital image. The FD is represented in mathematical form as:

$$\text{FD} = \log(N)/\log(r)$$

where, N = number of self-similar pieces and r = magnification factor. FD is calculated based on the box counting method. A low value of FD indicates presence of low noise level in the image [19].

The quality metrics for all images were calculated. The quality metrics values were plotted corresponding to each metrics separately depicted in Figs. 4A–4E. Quality metrics for the average filter were less than for the mixed filter and the median filter. However, the difference between the mixed filter and the median filter was less. Therefore, these data were analyzed further. The difference between median filter data and mixed filter data with respect to each quality metrics is calculated separately. From the data set, it was observed that quality metrics value for maximum difference, global contrast, AMBE, and FD favored the median filter. Hence it is inferred that the median filter is better than the mixed filter in performance. Therefore, the median filter was selected for further image analysis.

3.10. Image segmentation

Segmentation [20] involves separating an image into regions (or their contours) corresponding to objects. The regions are segmented based on common properties similarly contours by identifying differences between regions (edges). The simplest property that pixels in a region can share is intensity. Hence, such regions are segmented through thresholding, the separation of light and dark regions. Thresholding creates binary images from gray-level ones by turning all pixels below some threshold to zero and all pixels about that threshold to one. If $g(x, y)$ is a threshold version of $f(x, y)$ at some global threshold T , mathematically it is represented as:

$$g(x, y) = \begin{cases} 1 & \text{if } f(x, y) \geq T \\ 0 & \text{otherwise} \end{cases}$$

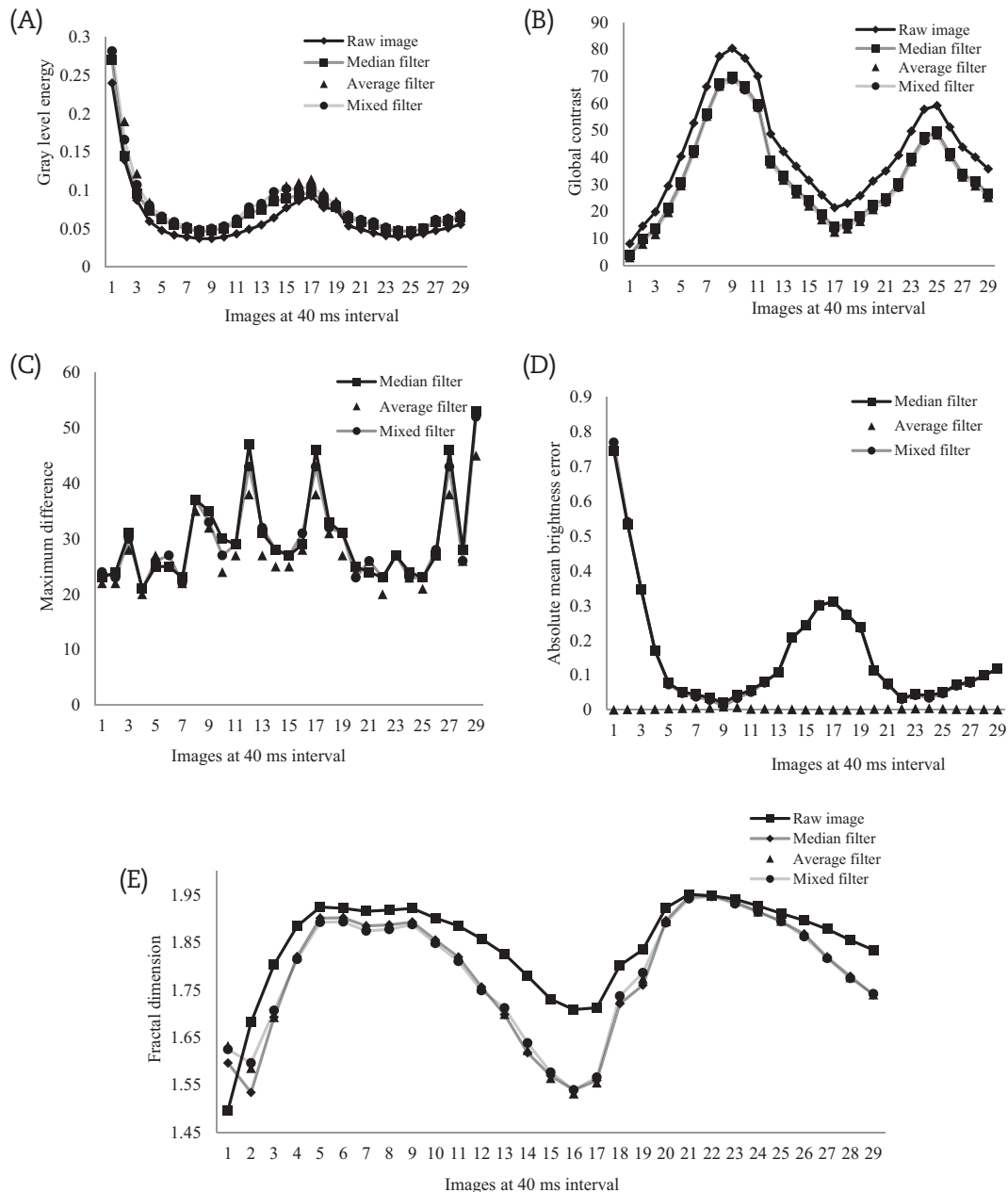


Fig. 4. Quality metrics values. (A) Gray level energy. (B) Global contrast. (C) Maximum difference. (D) Absolute mean brightness error. (E) Fractal dimension value for 29 images depicting the process.

The filtered image underwent segmentation using the histogram based thresholding method. The threshold for segmentation was been determined from the image histogram. The histogram of 29 images which depicts the process is shown in Fig. 5. The threshold gray level is selected as 7. Gray values above 7 represent the presence of woods metal.

The segmented image that underwent median filtering showed very good results as compared to the segmented image produced without filtering. Fig. 6 depicts the effect of the median filter in the removal of complex noises present in the image.

3.11. Contour identification using edge detection filter

The process of identifying and locating sharp discontinuities in an image is referred to as edge detection. Classical methods of edge detection involve convolving the image with an operator (two dimensional filter), which is constructed to be sensitive to large gradients in the image while returning values of zero in uniform regions. The contours of a jet profile can be extracted from segmented images. The edge detection is mainly grouped into two categories: gradient method and Laplacian. The gradient method detects the edges by looking for the maximum and minimum in the first derivative. Sobel, Prewitt, Robert edge detection is an example of the gradient method. These groups of edge detection filters are mainly comprised of specific filter masks or kernels. These kernels are applied separately to the input image to produce separate measurements of the gradient component in each orientation, i.e., horizontal and vertical directions (call these G_x and G_y). These can then be combined together to find the absolute magnitude of the gradient at each point and the orientation of that gradient. The gradient magnitude is given by:

$$|G| = \sqrt{G_x^2 + G_y^2}$$

An approach used frequently is to approximate the magnitude of the gradient by absolute values:

$$|G| = |G_x| + |G_y|$$

This equation is more attractive computationally, and it still preserves relative changes in intensity levels.

Direction of gradient vector is given by the angle:

$$\alpha(x,y) = \tan^{-1} \left(\frac{G_y}{G_x} \right)$$

Roberts:

G_x		
−1		0
0		+1
G_y		
−1		0
0		+1

Prewitt:

G_x		
−1	−1	−1
0	0	0
+1	+1	+1
G_y		
−1	0	+1
−1	0	+1
−1	0	+1

Sobel:

G_x		
−1	−2	−1
0	0	0
+1	+2	+1
G_y		
−1	0	+1
−2	0	+2
−1	0	+1

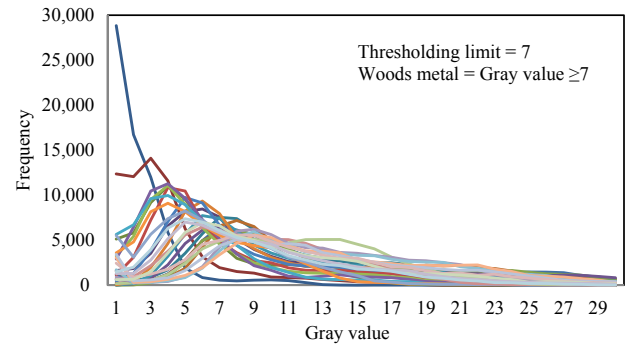


Fig. 5. Histogram of processed images.

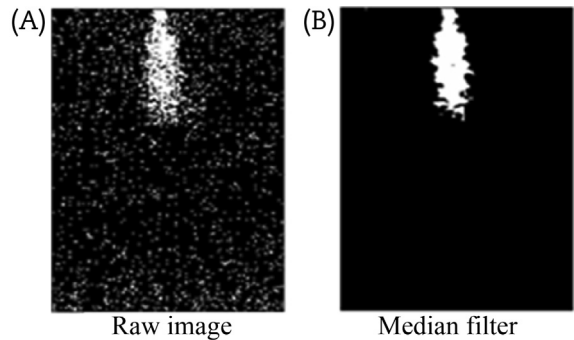


Fig. 6. Segmented images. (A) Without median filter. (B) With median filter.

The Laplacian method searches for zero crossings in the second derivative of the image to find edges. The Laplacian of Gaussian (log) filter is based on Laplacian method:

$$\Delta^2 f = \frac{\partial^2 f}{\partial x^2} + \frac{\partial^2 f}{\partial y^2}$$

Canny edge detection smooths the input image with a Gaussian filter then computes the gradient magnitude and the angle images. It applies non maxima suppression to the gradient magnitude image and uses double thresholding and connectivity analysis to detect and link edges.

The images are filtered using Sobel, Canny, Log, Prewitt, and Robert edge filters. Fig. 7 depicts performances of different filters for an image at 80 milliseconds. It was observed that the canny edge detection filtered image provided excellent results in comparison to other filters.

3.12. Determination of jet breakup length

The molten metal jet breaks up due to thermal and hydrodynamic instability during solidification as it travels through the coolant pool. The liquid jet composed of molten core material

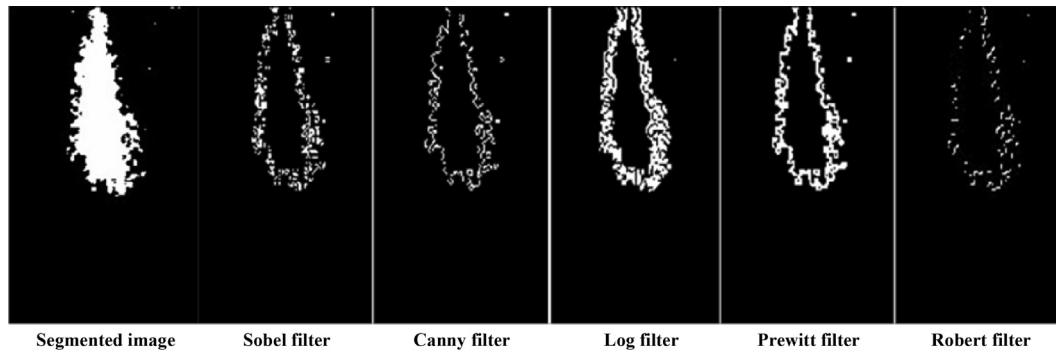


Fig. 7. Performance of different edge detection filters on a segmented image.

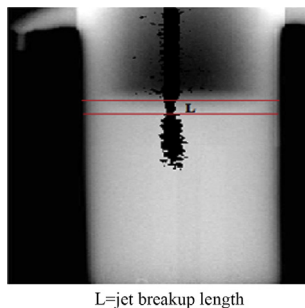


Fig. 8. Jet breakup length inside the water column.

breakup length and diameter of fragmented molten jet helps us to predict the solidification behavior of core material in a coolant pool after a core disruptive accident. Jet breakup is observed at $t = 40$ milliseconds after the interaction. Hence, in order to calculate jet breaking length, the dimension of the tank was used for calibration purposes. The image was segmented and added arithmetically with the image at $t = 0$ milliseconds. A complement of the added image was obtained, which is shown in Fig. 8. The jet breakup length is shown in Fig. 8 using two straight horizontal lines. This jet breakup is defined as the sudden reduction in the jet diameter during its

interaction with coolant. The jet diameter and breakup length were calculated as 4.73 mm and 10.6 mm, respectively. Jet breakup length was calculated as 58.45 mm and 73.55 mm for Saito's correlation and Epstein's correlation [3], respectively. A large difference was observed between the theoretical value of jet breakup length and the value which resulted from the experiment. These deviations of the experimental data could be due to the differences in flow characteristics of the water jet into Freon-11 and liquid nitrogen as compared to the woods metal water system [3]. In the Epstein's correlation, the entrainment of the jet into the other fluid is assumed to be proportional to the difference in velocity and the balance of the forces acting on the fragmenting drop. However, in the present experiment, woods metal is dropped from 300 mm above the water interface and the jet remains in the air column for some time. The jet diameter at the fluid interface is considered as the characteristic dimension to calculate the jet break up length.

3.13. Determination of jet front displacement with time

The jet velocity is described in three regions. In the first region, the jet velocity increases, whereas in the second region it decreases with the final phase, and in the third region, it remains steady [3]. The jet velocity was calculated from the segmented X-ray images. In order to calculate underwater jet front velocity, the

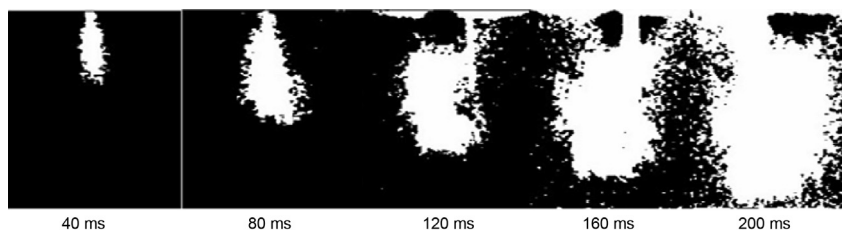


Fig. 9. Segmented image using 5×5 size averaging filter.

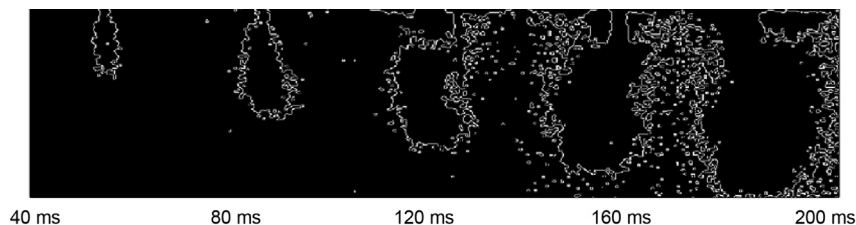


Fig. 10. Canny edge detection results.

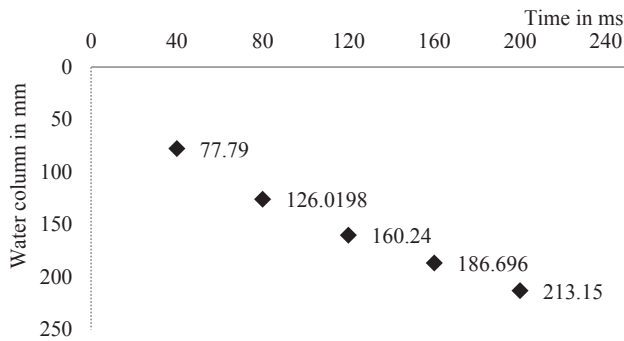


Fig. 11. Jet axial displacement (± 1.28 mm) versus time plot.

Table 2
Jet front velocity versus time.

Velocity (m/sec)	Time (millisec)
1.205	80
0.855	120
0.661	160
0.661	200

images are cropped in 210×330 size. The cropped images are processed using a median filter. The segmented images at different time intervals from 40 milliseconds to 200 milliseconds are depicted in Fig. 9.

The images depicting edges of jet profiles were obtained using a canny edge detection filter as shown in Fig. 10. This figure shows that the jet contact area increases at every 40 milliseconds. The canny filter provided optimized results for the segmented images. The bright pixels depict the woods metal jet contour within the water column in Fig. 10. The jet front position was calculated after

calibrating the image. The jet front axial displacement versus time plot derived from the segmented image is shown in Fig. 11. These processed images help us to understand the evolution of jet pattern.

It was observed that the velocity of front jet decreased as it hit the water surface and it further decreased until 213.15 mm depth of water column as presented in Table 2. The relative velocity observed between woods metal and water shows hydrostatic fragmentation.

3.14. Vapor phase detection

The temperature difference between melt (200°C) and water (30°C) was maintained in order to generate enough super heat for vapor generation. The vapor phase was captured by the DFPD. The vapor bubbles observed in images acquired at 0.76–0.96 s are shown in Fig. 12A. Interpretation of bubble shape from raw images is very difficult. The vapor bubble formed during interaction is depicted in Fig. 12B. The peaks observed in the plot profile indicate the presence of high gray value within the water column and this confirms the presence of bubbles in the pool.

Fig. 13 depicts the movement of bubbles inside the water column in 40 millisecond intervals. These processed images were studied and a plot between bubble position (bubble bottom part has been taken as reference) and time was drawn. The bubble velocity was measured using the plot depicted in Fig. 14. The obtained velocity values are represented in Table 3.

A large temperature difference leads to vapor formation. The formed vapor expands in the water. The reaction force exerted by liquid due to increased volume of vapor contributes to the large velocity change of vapor in a short time. It has been observed at time 0.76 s bubble formation takes place due to superheating of water. The energy produced is visible through

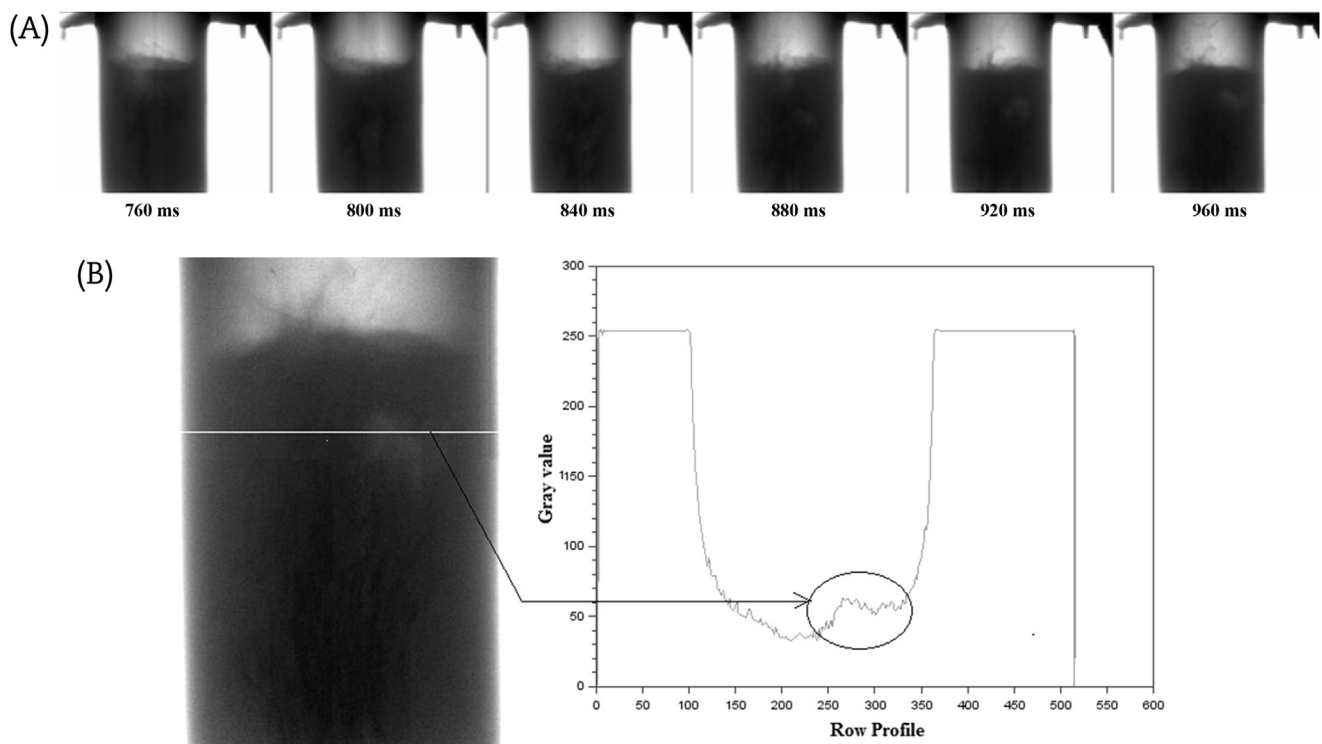


Fig. 12. Vapor bubbles. (A) Raw images showing the presence of bubbles. (B) Row profile showing the presence of vapor bubbles at 0.96 s.

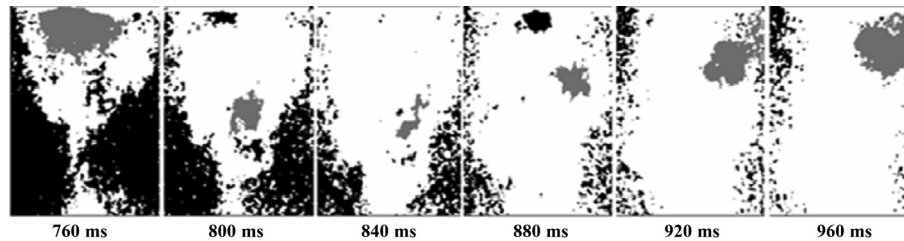


Fig. 13. Depicting bubble movement inside the water column.

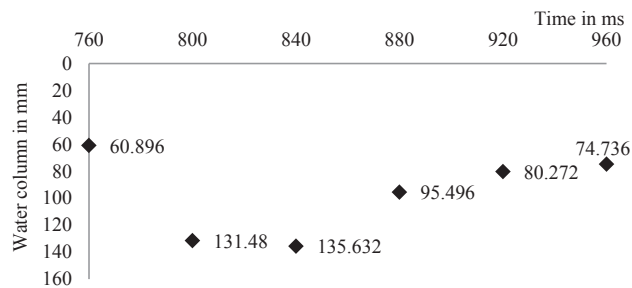


Fig. 14. Bubble displacement (± 1.28 mm) versus time plot.

Table 3
Bubble velocity versus time.

Velocity (m/sec)	Time (sec)
1.75 (down)	0.76
0.1158 (down)	0.80
1.0034 (up)	0.84
0.3806 (up)	0.88
0.1384 (up)	0.92

bubble velocity which travelled 70.104 mm downward in the water column in 40 millisecond intervals. Bubble velocity changes to 0.1158 m/s from 1.75 m/s were seen after losing energy to the contained medium. After this, the bubble was seen moving up to the water surface.

4. Conclusion

This study deals with development of a technique to depict MFCI phenomena using real time radiography in an opaque medium. An algorithm for image enhancement of the raw images (obtained from the experiment) was developed. There was significant improvement in the obtained raw images. The median filter was found to be useful in reducing random noise. The histogram based thresholding method produced the desired results well within the limit. This helped us to clearly visualize the woods metal interaction inside water. The attributes of the MFCI process, including jet breakup length, jet front axial displacement, and vapor phase displacement, were calculated from the processed image. It was observed that the DFPD screen size limits the view of the process. However, the covered area was able to access important events that occurred in an MFCI. This experiment brings out salient features of post image analysis.

Conflicts of interest

All authors have no conflicts of interest to declare.

Acknowledgments

Authors acknowledge the support given by Shri N Raghu, Shri P. Narayana Rao and officials of Quality Assurance Division (QAD), Health, Safety & Environment Group (HSEG) of Indira Gandhi Centre for Atomic Research (IGCAR), Kalpakkam for carrying out radiographic operations.

References

- [1] A.E. Waltar, A.B. Reynolds, *Fast Breeder Reactors*, Pergamon Press, USA, 1981.
- [2] H.S. Park, R.C. Hanson, B.R. Sehgal, Continuous high speed X-ray radiography to visualize dynamic fragmentation of molten liquid droplet in liquid coolant, in: *Proceedings of PSFVIP-4*, June 3–5, 2003. Chamonix, France, F4090.
- [3] Eiji Matsuo, Yutaka Abe, Keiko Chitose, Kazuya Koyama, Kazuhiro Itoh, Study on jet breakup behaviour at core disruptive accident for fast breeder reactor, *Nucl. Eng. Des.* 238 (2008) 1996–2004.
- [4] R.C. Hansson, Triggering and energetics of a single drop vapour explosion: the role of entrapped non-condensable gases, *Nucl. Eng. Technol.* 41 (2009) 1215–1222. Special Issue on the 7th International Topical Meeting on Nuclear Reactor Thermal Hydraulics, Operation, and Safety.
- [5] M. Zabiego, C. Brayer, D. Grishchenko, J.-B. Dajon, P. Fouquart, Y. Bullado, F. Compagnon, P. Correggio, J.-F. Haquet, P. Piluso, The KROTOS KFC and SERENA/KS1 tests: experimental results and MC3D calculations, in: *7th International Conference on Multiphase Flow ICMF 2010*, Tampa, FL USA, 30–June 4, 2010.
- [6] A.R. Potter, J.C. Austin, R.M. Ormerod, P.W. Haycock, B.R. Heywood, S.D. George, X-ray images of defect formation in porcelain ceramics during drying, *NDT E Int.* 36 (2003) 77–83.
- [7] E.P. Loewen, R. Bonazza, M.L. Corradini, R.E. Johannesen, Fuel – coolant interactions: visualisation and mixing measurements, *Nucl. Technol.* 139 (2002) 127–144.
- [8] P. Munshi, P. Jayakumar, P. Satyamurthy, T.K. Thiyagarajan, N. Venkatramani, Void-fraction measurements in a steady-state mercury nitrogen flow loop, *Exp. Fluids* 24 (1998) 424–430.
- [9] R. Saksena, P. Satyamurthy, P. Munshi, A comparison of experimental results and FLUENT simulations for void-fraction distribution in a two-phase system, *Nucl. Technol.* 163 (2008) 426–434.
- [10] Available from: <http://physics.nist.gov/PhysRefData/XrayMassCoef/ElemTab/z11.html>.
- [11] Available from: <http://physics.nist.gov/PhysRefData/XrayMassCoef/ComTab/water.html>.
- [12] F.C. Campbell, *Inspection of Metals – Understanding the basics*, copyright 2013, ASM International, p.233–261.
- [13] R.C. Gonzalez, R.E. Woods, *Digital Image Processing*, Prentice Hall, USA, 2002.
- [14] M. Sonka, V. Hlavac, R. Boyle, *Image Processing, Analysis, and Machine Vision*, second ed., Thomson Learning, USA, 2008.
- [15] E.L. Hall, R.P. Kruger, S.J. Dwyer, D.L. Hall, R.W. McLaren, G.S. Lodwick, A survey of preprocessing and feature extraction techniques for radiographic images, *IEEE Trans. Comput.* c-20 (1971) 1032–1044.
- [16] Scilab manuals. http://www.scilab.org/download/5.1.1/manual_scilab-5.1.1_en_US.pdf.
- [17] J. Majumdar, A. Manikonda, G.M. Venkatesh, Adaptive enhancement of underwater images, in: *ICSIP 2012*, Lecture Notes in Electrical Engineering, vol. 221, Springer India, 2013, http://dx.doi.org/10.1007/978-81-322-0997-3_50.
- [18] P. Athe, S. Shakya, P. Munshi, A. Luke, D. Mewes, Characterization of multiphase flow in bubble columns using kt-1 signature and fractal dimension, *Flow Meas. Instrum.* 33 (2013) 122–137.
- [19] T. Pant, Effect of noise in estimation of fractal dimension of digital images, *Int. J. Signal Process. Image Process. Pattern Recognit.* 6 (2013) 101–116.
- [20] Available from: http://homepages.inf.ed.ac.uk/rbf/CVonline/LOCAL_COPIES/MORSE/threshold.pdf.